NASA Technical Memorandum 83636

Analysis of Inviscid and Viscous Flows in Cascades with an Explicit Multiple-Grid Algorithm

Rodrick V. Chima
Lewis Research Center
Cleveland, Ohio

Prepared for the
Seventeenth Fluid Dynamics, Plasma Dynamics, and Lasers Conference
sponsored by the American Institute of Aeronautics and Astronautics
Snowmass, Colorado, June 25-27, 1984

NASA

E-2078

ANALYSIS OF INVISCID AND VISCOUS FLOWS IN CASCADES WITH AN EXPLICIT MULTIPLE-GRID ALGORITHM

Rodrick V. Chima
National Aeronautics and Space Administration
Lewis Research Center
Cleveland, Ohio 44135

Abstract

A rapid technique has been developed for calculating inviscid and viscous flows in turbomachinery cascades. The Euler and thin-layer Navier-Stokes equations are solved using the original explicit MacCormack algorithm. The Baldwin-Lomax eddy viscosity model is used for turbulent flows. Convergence to a steady state is accelerated by use of a variable time-step and a multiple-grid scheme. Computer time is reduced through vectorization. Details of the numerical method are presented along with computed results for two low-speed wind tunnel turning vanes, a space shuttle fuel pump turbine rotor, and a supersonic inflow compressor rotor. Results show that the method can predict subtle viscous flow phenomena in cascades and is fast enough to be used as a design tool.

Introduction

Flows in turbomachinery blade passages are often highly rotational and may be dominated by shock waves or viscous effects. For example, fan blades and compressor rotors often see a supersonic relative inflow that causes a strong shock-wave system. They may even operate with a choked massflow. Compressors are designed specifically to produce an adverse pressure gradient which causes boundary layer thickening and often flow separation. Turbine blades on the other hand may accelerate a low-speed flow to supersonic speeds. Although the resulting pressure gradients are generally favorable, local recirculation regions can occur that lead to hot spots and possible failure. Yet most of the turbomachinery blade design work done today relies on subsonic analyses (e.g. 1) or transonic potential analyses (e.g. 2). Although Navier-Stokes analyses have been developed for cascades (e.g. 3 or 4), they tend to be computationally inefficient.

The goal of the present work is the development of a fast Euler and Navier-Stokes cascade analysis code that can be used in a design environment. The code is based on the original explicit MacCormack algorithm[5] which is widely used and well-understood, but can be slow. Efficiency is achieved by three means: by vectorization, by use of a variable time step, and by use of a multiple-grid acceleration scheme developed by Ni[6] and adapted to the MacCormack algorithm by Johnson.[7]

Governing Equations

The two-dimensional unsteady thin-layer Navier-Stokes equations may be written in fully conservative form for an arbitrary coordinate system as follows:

$$\partial_t \hat{q} + \partial_\varepsilon \hat{E} + \partial_\eta (\hat{F} - Re^{-1} \hat{S}) = 0 \tag{1}$$

where

$$\hat{q} = J^{-1}\begin{bmatrix}\rho\\ \rho u\\ \rho v\\ e\end{bmatrix} \quad \hat{E} = J^{-1}\begin{bmatrix}\rho U\\ \rho uU + \varepsilon_x p\\ \rho vU + \varepsilon_y p\\ (e+p)U\end{bmatrix} \quad \hat{F} = J^{-1}\begin{bmatrix}\rho V\\ \rho uV + \eta_x p\\ \rho vV + \eta_y p\\ (e+p)V\end{bmatrix} \tag{2}$$

$e = \rho\left[C_v T + 1/2\ (u^2 + v^2)\right]$ is the total energy per unit volume

and

$p = (\gamma - 1)\left[e - 1/2\ \rho\ (u^2 + v^2)\right]$ is the static pressure

The viscous flux term is expressed as:

$$\hat{S} = J^{-1}{}_u\begin{bmatrix}0\\ C_1\partial_\eta u + C_2\partial_\eta v\\ C_2\partial_\eta u + C_3\partial_\eta v\\ C_4\partial_\eta\left[e/\rho - 1/2\ (u^2+v^2)\right]\\ \quad + (C_1 u + C_2 v)\partial_\eta u + (C_2 u + C_3 v)\partial_\eta v\end{bmatrix} \tag{3}$$

where

$$C_1 = 1^{1/3}\eta_x^2 + \eta_y^2; \qquad C_2 = 1/3\ \eta_x\eta_y;$$

$$C_3 = \eta_x^2 + 1^{1/3}\eta_y^2; \qquad C_4 = (\gamma/Pr)(\eta_x^2 + \eta_y^2)$$

In Eqs. (1) to (3) J is the transformation Jacobian:

$$J = \varepsilon_x\eta_y - \varepsilon_y\eta_x = 1/(x_\varepsilon y_\eta - x_\eta y_\varepsilon) \tag{4}$$

Metric quantities are determined from a finite-difference grid using central differences and:

$$\varepsilon_x = Jy_\eta;\ \varepsilon_y = -Jx_\eta;\ \eta_x = -Jy_\varepsilon;\ \eta_y = Jx_\varepsilon \tag{5}$$

The contravariant velocity components U and V along the ε and η grid lines are given by:

$$U = \varepsilon_x u + \varepsilon_y v;\ V = \eta_x u + \eta_y v \tag{6}$$

The equations are nondimensionalized by arbitrary reference quantities (here the inlet total

density and critical sonic velocity are used), and the Reynolds number Re and the Prandtl number Pr must be specified in terms of those quantities. These equations assume that the specific heat Cp and Prandtl number are constant, that Stokes' hypothesis $\lambda = -2/3\ \mu$ is valid, and that the effective viscosity may be written as:

$$\mu = \mu_{laminar} + \mu_{turbulent}$$

To allow eventual calculation of heat transfer to turbine blades the energy equation is included. The thin-layer assumption has been invoked to eliminate streamwise viscous derivatives, thereby reducing computational overhead while retaining the capability of computing separated flows.

For turbulent flows the algebraic two-layer eddy viscosity model developed by Baldwin and Lomax[8] is used. Their subroutine was recoded for vectorization on a Cray I-S computer. In this work the turbulence model was applied on an expanding C-shaped region of the grid that starts near the leading edge and grows to cover the entire wake region near the trailing edge. Limiting the model to this region eliminates problems caused by numerically-generated vorticity that is ocassionally calculated in coarse upstream regions of the grid.

Computational Grid

Body-fitted grids for this work have been generated using the GRAPE code (GRids about Airfoils using Poisson's Equation) developed by Sorenson.[9,10] Briefly, the code allows arbitrary specification of inner and outer boundaries, then generates interior points as a solution to a Poisson equation. Forcing terms in the Poisson equation are chosen such that desired grid spacing and grid angles may be maintained at the inner and outer boundaries. Sorenson's inner boundary subroutine was modified to allow a more general clustering of points about leading and trailing edges of highly-cambered turbomachinery blades. His outer boundary subroutine was modified to improve generation of the periodic boundaries in high-solidity blade rows. The grids used in this work are C-shaped and are periodic over the pitch of a given cascade.

Boundary Conditions

At the cascade inlet, total pressure, total temperature, and either the flow angle α_{in} or the y-velocity component v_{in} are specified. In either case u_{in} is computed as part of the solution using a characteristic boundary condition similar to Jameson's.[11] Here the upstream-running Riemann invariant R^- based on the total velocity Q is extrapolated from the interior to the inlet:

$$R^-_{in} = \left[Q - \frac{2C}{\gamma - 1}\right]_{extrapolated}$$

where

$$C = \sqrt{\frac{\gamma p}{\rho}} \text{ is the sonic velocity} \qquad (7)$$

Then using the known total temperature T_0 and the isentropic relations:

$$Q_{in} = \left[\frac{(\gamma - 1)R^- + \sqrt{4(\gamma + 1)\, C_p T_0 - 2(\gamma - 1)(R^-)^2}}{(\gamma + 1)}\right]_{in} \qquad (8)$$

Individual velocity components are found from trigonometric relations, and pressure and density are found from isentropic relations.

For subsonic inflow either α_{in} or v_{in} may be specified, although it is usually more convenient to specify the angle. For purely supersonic inflow (uncommon in tubomachinery) all four conservation variables must be specified at the inlet. But for flows in which the total velocity Q_{in} is supersonic while the axial component u_{in} is subsonic, v_{in} must be specified. This is often the case with compressor rotors, where the rotation may be accounted for by setting v_{in} equal to the inlet whirl minus the wheel speed. It is numerically possible to specify α_{in} for this case; however, the algorithm converges to the fully-subsonic solution with the specified α_{in} but low values of wheel speed and mass flow.

For inviscid flows the exit boundary condition is also a variation of Jameson's characteristic treatment.[11] Here the upstream-running Riemann invariant R^- based on the x-velocity component u is specified. The downstream-running Riemann invariant R^+, the y-velocity component v and the total pressure P_0 are extrapolated from the interior. Thus at the exit:

$$R^-_{out} = \left[u - \frac{2C}{\gamma - 1}\right]_{out} \text{ is specified} \qquad (9)$$

$$R^+_{out} = \left[u + \frac{2C}{\gamma - 1}\right]_{out} \text{ is extrapolated} \qquad (10)$$

Eqs. (9) and (10) are solved for u_{out} and C_{out}, which are combined with the extrapolated y-velocity component v_{out} to give the exit Mach number. Then the total pressure is extrapolated from the interior and the exit static pressure is found from the isentropic relations.

For viscous flows the exit Riemann invariant R^- is not constant across the wake, so the characteristic treatment is abandoned in favor of a specified static pressure and extrapolations of the other conservation variables. Although this is a reflective boundary condition it does not seem to be a limiting factor on convergence rate.

On the blade surfaces flow tangency is enforced for inviscid flow by extrapolating U and setting V = 0. For viscous flow u = v = 0. Surface pressures are computed using the normal momentum equation:

$$(\eta_x \epsilon_x + \eta_y \epsilon_y) p_\epsilon + (\eta_x^2 + \eta_y^2) p_\eta = -\rho U(\eta_x u_\epsilon + \eta_y v_\epsilon) \qquad (11)$$

where U = 0 on the surface for viscous flows.

Surface densities are found from surface pressures and a specified wall temperature. For inviscid flow the wall temperature is found from the surface velocities and the surface total temperature, which must equal the inlet total temperature in the steady state. This boundary condition is sometimes unstable at blunt trailing edges in inviscid flows. In this case it is replaced by a boundary condition suggested by Barton and Pulliam.[12] Here the entropy; expressed as p/ρ^{γ}, is extrapolated to the surface and used to find the density. This wall boundary condition is very stable, does not guarantee constant wall total temperature, but does tend to improve total pressure (or entropy) conservation as reported in Ref. (12).

Fine-Grid Algorithm

On the fine grid the explicit MacCormack algorithm is used in its unsplit form.[5] MacCormack's algorithm is a particularly popular member of the class of Lax-Wendroff two-step schemes. It is given below in its forward predictor-backward corrector form.

Governing Equations

$$\partial_t \hat{q} = -\left[\partial_\xi \hat{E} + \partial_\eta (\hat{F} - Re^{-1}\hat{S})\right] \tag{7}$$

Store Current Solution in array $\Delta\hat{q}$

$$\Delta\hat{q}^n_{i,j} = \hat{q}^n_{i,j} \tag{11}$$

Forward Predictor

$$\hat{q}^*_{i,j} = \hat{q}^n_{i,j} - \Delta t_{i,j}\left[(\hat{E}_{i+1,j} - \hat{E}_{i,j}) + (\hat{F}_{i,j+1} - \hat{F}_{i,j}) - Re^{-1}(\hat{S}_{i,j+1} - \hat{S}_{i,j})\right] \tag{12}$$

Backward Corrector

$$\hat{q}^{n+1}_{i,j} = 1/2\left\{\hat{q}^n_{i,j} + \hat{q}^*_{i,j} - \Delta t^*_{i,j}\left[(\hat{E}^*_{i,j} - \hat{E}_{i-1,j}) + (\hat{F}^*_{i,j} - \hat{F}^*_{i,j-1}) - Re^{-1}(\hat{S}^*_{i,j} - \hat{S}^*_{i,j-1})\right]\right\} \tag{13}$$

Artificial Dissipation

$$\overline{\hat{q}^{n+1}_{i,j}} = \hat{q}^{n+1}_{i,j} + D_{i,j} \tag{14}$$

Collect Residuals in array $\Delta\hat{q}$

$$\Delta\hat{q}^{n+1}_{i,j} + \overline{\hat{q}^{n+1}_{i,j}} - \Delta\hat{q}^n_{i,j} \tag{15}$$

First derivatives in the viscous flux vector $\hat{S}$ are backward-differenced in the predictor and forward-differenced in the corrector. Eqs. (12) to (14) are differenced across the periodic cascade boundaries. Although this requires extra programming logic, it gives better solution accuracy and convergence rates than averaging schemes sometimes used to enforce periodicity. It is especially useful when shocks cross the periodic boundaries.

Artificial Dissipation

Dissipative terms consisting of second and fourth differences are added to prevent odd-even point decoupling and to allow shock capturing. The dissipative terms are similar to those used by Jameson[11] and others. A one-dimensional version is shown below. In two-dimensions the dissipation is added as a sequence of one-dimensional operators.

Fourth-Order Dissipation

$$D_{4i,j} = \nu_4 \Delta t_{i,j} J^{-1}_{i,j}\,(q_{i+2,j} - 4q_{i+1,j} + 6q_{i,j} - 4q_{i-1,j} + q_{i-2,j}) \tag{16}$$

where

$$\nu_4 = 0\ (0.5)$$

Second-Order Dissipation

$$D_{2i,j} = \nu_2 \nu_\rho J^{-1}_{i,j}\,(q_{i+1,j} - 2q_{i,j} + q_{i-1,j}) \tag{17}$$

where

$$\nu_\rho = \frac{\left|\rho_{i+1,j} - 2\rho_{i,j} + \rho_{i-1,j}\right|}{(\rho_{i+1,j} + 2\rho_{i,j} + \rho_{i-1,j})}$$

and

$$\nu_2 = 2\nu_4$$

Combined Dissipation

$$D_{i,j} = D_{2i,j} - D_{4i,j} = -\nu_4(q_{i+2,j} + q_{i-2,j}) + C_2\,(q_{i+1,j} + q_{i-1,j}) + C_0 q_{i,j} \tag{18}$$

where

$$C_2 \equiv V_2 + 2V_4;\ C_0 \equiv -2\,(V_2 + 3V_4)$$

$$V_2 \equiv \nu_2\,\nu_\rho / J_{i,j};\ V_4 \equiv \nu_4\,\Delta t_{i,j}\,/J_{i,j}$$

and the nomenclature is not to be confused with that used for the viscous flux vector.

In smooth regions of the flow the dissipative terms are within the truncation error of the MacCormack algorithm and thus do not detract from the formal accuracy of the fine-grid scheme. Second-order dissipation is usually added to prevent pre-shock oscillations. Here it has also been found to be important in preventing point decoupling on irregular upstream grids, even in fully subsonic flows. The second-order dissipation coefficient ν_ρ has been written in terms of the density rather than the commonly-used pressure for computational efficiency.

Variable Time-Step

A spatially-variable time-step $\Delta t_{i,j}$ is used in Eqs. (12), (13), and (16) to accelerate convergence of the fine-grid algorithm to steady state. Time steps are chosen at each grid point

such that the Courant number is constant everywhere, typically 0.9. Time steps are calculated from the inviscid stability limit based on the initial inlet conditions and are not updated during the calculations. Thus the time step varies as a function of grid spacing only. It is given by a variation of the time-step derived for general coordinates by Shang[13]:

$$\Delta t_{i,j} = \frac{CFL}{(dx|u| + dy|v| + C\sqrt{dx^2 + dy^2})} \quad \text{initial conditions} \qquad (19)$$

where

$$dx \equiv |\epsilon_x| + |\eta_x| \; ; \; dy \equiv |\epsilon_y| + |\eta_y|$$

and

CFL = Courant number.

Here the absolute value has been taken of each metric term to allow for metric sign changes on the C-grid.

Coarse-Grid Algorithm

Given the change in the fine-grid solution computed by one iteration of the MacCormack algorithm, successively coarser grids are used to propagate this change throughout the domain. The coarse-grid propagation scheme used here is essentially the second half of a one-step Lax-Wendroff scheme developed by Ni[6] for the Euler equations. The first step of Ni's scheme computes changes at a grid point, and the second step distributes those changes to surrounding points.

Johnson has shown that the first step of Ni's scheme may be replaced by a variety of Lax-Wendroff schemes, including MacCormack's scheme.[7] Furthermore, Johnson has demonstrated that in viscous flows dissipative effects have a local character and need not be modeled on the coarse grids.[14] Thus the so-called "convective coarse-grid acceleration scheme" used here is based solely on the Euler equations. The coarse-grid algorithm is entirely independent of the viscous terms retained, the turbulence model used, or any artificial dissipation added on the fine grid.

The coarse-grid algorithm is written in general coordinates as:

$$\begin{aligned}\delta\hat{q}_{i,j} = 1/4 \Big\{ &\left[\Delta\hat{q} + \Delta t_{i,j}(\Delta\hat{E} + \Delta\hat{F})\right]_{i-1,\, j-1} \\ &+ \left[\Delta\hat{q} + \Delta t_{i,j}(\Delta\hat{E} - \Delta\hat{F})\right]_{i-1,\, j+1} \\ &+ \left[\Delta\hat{q} + \Delta t_{i,j}(-\Delta\hat{E} - \Delta\hat{F})\right]_{i+1,\, j+1} \\ &+ \left[\Delta\hat{q} + \Delta t_{i,j}(-\Delta\hat{E} + \Delta\hat{F})\right]_{i+1,\, j-1} \Big\} \end{aligned} \qquad (20)$$

where

$$\Delta\hat{E}_{i+1,\, j+1} \equiv \hat{A}_{i+1,\, j+1}\, \Delta\hat{q}_{i+1,\, j+1};$$

$$\Delta\hat{F}_{i+1,\, j+1} \equiv \hat{B}_{i+1,\, j+1}\, \Delta\hat{q}_{i+1,\, j+1}; \qquad (21)$$

$$\hat{A} = \epsilon_x A + \epsilon_y B \; ; \; \hat{B} = \eta_x A + \eta_y B$$

and A and B are the Jacobian matrices of the Cartesian flux vectors given by:

$$A \equiv \frac{\partial E}{\partial q} = \begin{bmatrix} 0 & 1 & 0 & 0 \\ \phi^2 - u^2 & (3-\gamma)u & (1-\gamma)v & \gamma-1 \\ -uv & v & u & 0 \\ (2\phi^2 - \gamma e/\rho)u & \gamma e/\rho - \phi^2 - (\gamma-1)u^2 & (1-\gamma)uv & \gamma u \end{bmatrix}$$

$$B \equiv \frac{\partial F}{\partial q} = \begin{bmatrix} 0 & 0 & 1 & 0 \\ -uv & v & u & 0 \\ \phi^2 - v^2 & (1-\gamma)u & (3-\gamma)v & \gamma-1 \\ (2\phi^2 - \gamma e/\rho)v & (1-\gamma)uv & \gamma e/\rho - \phi^2 - (\gamma-1)v^2 & \gamma v \end{bmatrix}$$

and

$$\phi^2 \equiv \frac{\gamma - 1}{2}(u^2 + v^2)$$

The fine grid must be chosen such that the number of points in each direction is expressible as $n(2^p) + 1$ for n and p integers where $p \geq 0$ is the number of grid coarsenings and $n \geq 2$ is the number of intervals on the coarsest grid. Coarse grids are defined by successive deletion of every other grid line in each coordinate direction.

Fine-grid changes $\Delta\hat{q}_{i,j}$ are restricted to coarser grids by injection. Eqs. (20) to (22) are used to compute corrections $\delta\hat{q}$ at coarse-grid points (i,j) based on data at neighboring coarse-grid points $(i \pm l,\ j \pm l)$, where $l = 1,2,4,8, \ldots (2)^{\text{grid number}-2}$ is the coarse-grid spacing. Coarse-grid corrections are prolonged back to the fine grid using bilinear interpolation.

Vectorization

It is well known that explicit algorithms in general and MacCormack's algorithm in particular are highly vectorizable (e.g. 15). The multiple-grid scheme presented here is explicit and is also fully vectorizable, although efficiency does decrease with vector length on the coarsest grids. Details on vectorization of the multiple-grid algorithm were presented in Ref. 16. All of the results presented in the following section were computed with a fully vectorized code run on a Cray I-S computer. The code was redimensioned for each grid size run, and required 400 K words of memory for the largest grid (161 x 41 points).

Results

Four cascades with widely-varying flow conditions have been analyzed both inviscidly and viscously with the explicit multiple-grid code. The following examples are presented to demonstrate the utility of this code. The first and second examples are cascades of low-speed wind tunnel turning vanes. The third example is a turbine blade used in a fuel turbopump on the space shuttle. The final example is a compressor rotor with supersonic relative inflow.

Figures 1 to 6 show computational results for a cascade of corner vanes designed for NASA Ames Research Center's (ARC) 40' x 80' or 80' x 120' subsonic wind tunnel. Two sets of the original corner vanes were redesigned by E.R. McFarland of

NASA Lewis Research Center (LeRC) and are to be replaced while the tunnel is down for completion of the 80' x 120' leg. The redisgned vanes have a chord of 7.2 feet and a span of 80 feet, so the flow is predominantly two-dimensional. The inlet Mach number is approximately 0.23. The blades have been tested at one-tenth scale in an eight-vaned cascade tunnel at ARC with a scale chord Reynolds number of one million.

Figure 1 shows the periodic C-type grid used for the corner vane problem. The inviscid grid (shown) has 113 x 25 points with an initial spacing away from the body of 0.0035 chord. The viscous grid had 113 x 33 points with an initial spacing of 0.00035 chord.

Convergence histories for the inviscid case as shown in Fig. 2, which plots the log of the maximum residual in the x-momentum equation versus iteration for three forms of the MacCormack algorithm. For the following discussion, convergence is taken to be a three-decade drop in this residual. The unmodified algorithm is limited by a small time step controlled by the small grid spacing near the body, and requires about 23 200 steps to converge. This takes about 500 sec on the Cray I-S. With a variable time-step the scheme converges in 7020 steps. This takes 152 sec for a work reduction factor of 3.27. With a variable time-step and four multiple-grid levels the scheme converges in 2030 steps. This takes 70.0 sec for a overall work reduction factor of 7.15. It is emphasized that the three schemes converge to identical solutions. A viscous turbulent solution on the finer 113 x 33 grid was computed using a variable time-step and three multiple-grid levels. It converged in 1840 time steps taking 155 sec.

Mach number contours shown in Fig. 3 for inviscid flow and in Fig. 4 for viscous flow show an interesting feature of this cascade. The blade surfaces are circular arcs designed such that the passage between two blades has concentric circular walls. The flow in this passage is nearly a free vortex, as indicated by the nearly-concentric Mach number contours. The inviscid mass-averaged exit flow angle is -45.12°, somewhat lower than the -48.7° angle of the mean camber line. The viscous exit flow angle is -43.47° which agrees well with a measured value of -43°.

Each example presented here was computed by iteratively varying the exit Riemann invariant for inviscid flow or the exit static pressure for viscous flow until the computed mass-flow rate equalled the design value. Viscous boundary layers present an increased blockage to a flow so that a viscous case requires a lower exit pressure to produce the same mass-flow rate as its inviscid equivalent. Simply put, a real compressor produces a lower pressure rise than an ideal compressor. For the corner vanes the viscous solution has a mass-averaged overall pressure ratio that is 0.074 percent lower than the inviscid solution.

The surface total pressure distribution is shown in Fig. 5 for the Euler solution. Referenced to the inlet total pressure it should be constant and equal to 1. The numerical error is less than 0.5 percent everywhere except for spikes at the leading-and-trailing-edges.

Surface static pressure distributions are shown in Fig. 6. The dashed line representing the Euler solutions compares well with a solution (circles) from a panel code by McFarland.[17] The viscous analysis was made at a Reynolds number of one-million, corresponding to the one-tenth scale model tested experimentally. The viscous solution (squares and triangles) has lower surface pressures than the inviscid solution due to boundary layer blockage. It agrees well with measured data (diamonds) on the pressure surface but is off on the suction surface. Experimental oil-streak data seem to indicate turbulent flow on the pressure surface but laminar flow on most of the suction surface. The Navier-Stokes calculations were essentially turbulent everywhere, which may account for the disagreement on the suction surface.

Figures 7 to 12 show results for a cascade of turning vanes designed by Sanz et al.,[18] also for the ARC wind tunnel. The cascade sits at the junction of the 80' x 120' leg and the 40' x 80' leg of the tunnel and directs the flow into the drive fans. The cascade has an inlet Mach number of about 0.19. It has also been tested at one-tenth scale at ARC with a scale chord Reynolds number of about 700 000. The inviscid grid used for the following results had 145 x 25 points and is shown at the top of Fig. 7.

This turning vane is rather unique in that it must operate over a 45° range of incidence angles. In the 80' x 120' mode the cascade receives flow from the 80' x 120' leg at 20.6° incidence and turns the flow 45°. This is illustrated by the viscous velocity vector plot at the bottom of Fig. 7. A small reverse flow region is apparent on the suction surface. In the 40' x 80' mode the cascade receives flow at -25.6° incidence and does not turn the flow. This is illustrated by the vector plot Fig. 8. A long but thin suction-surface separation is evident in the printout for this case.

Figures 9 and 10 show Mach number contours for the turning (80' x 120') and nonturning (40' x 80') cases respectively. The motion of the stagnation point around the nose is evident. Some underturning of the wake is evident in Fig. 9.

Surface pressure distributions are compared in Fig. 11 for the turning case. Here the Euler solution agrees well with a solution from McFarland's panel code (circles). The Navier-Stokes solution for the scale model Reynolds number (squares and triangles) is displaced below the inviscid solutions again because of viscous blockage, resulting in a viscous pressure ratio 0.53 percent lower than then the inviscid pressure ratio. Experimental pressure measurements from vane six of the eight-vaned cascade (diamonds) agree quite well with the Navier-Stokes solution.

Similar comparisons of surface pressures are made in Fig. 12 for the nonturning case. Here the roughly-equal areas under the curve on either side of 28 percent chord cancel so that no net lift is produced by the vane. Again the Euler and panel solutions agree well. The viscous pressure ratio was 0.42 percent lower than the inviscid. The viscous solution does not agree as well with the experimental data as in the previous case.

The turning vane solution were all run 5000 cycles using three multiple-grid levels. This resulted in a 4-1/2 decade drop in the residuals. Inviscid solutions took 213 sec on a 145 x 25 grid and viscous solutions took 518 sec on a 145 x 33 grid.

Figures 13 to 18 show results for the first-stage turbine rotor blade of the space shuttle fuel pump. This blade operates in a hydrogen-rich superheated steam environment at 357 atmospheres pressure and 1042 K (1876 R) temperature. The flow accelerates from an inlet Mach number of 0.23 to an exit Mach number of about 0.5. The axial chord of 1.86 cm (0.7323 in) gives a Reynolds number of four-million based on the inlet velocity. In the calculations the ideal gas constant, specific heats, and Sutherland viscosity constants were set to values for H_2.

Figures 13 shows the invisid grid of 113 x 25 points for this blade. The initial grid spacing away from the body is about 0.006 chord. The viscous grid had 113 x 41 points with an initial spacing of 1/70th of the inviscid spacing. Euler and turbulent Navier-Stokes calculations were each run 5000 cycles with three multiple-grid levels. The inviscid solution took 165 sec and the viscous solution took 455 seconds.

Figure 14 compares computed surface pressure distributions. The Euler solution (dashed) compares very well with a panel code solution (circles) except for the suction-surface recompression near the trailing edge where the panel code compressibility correction is slightly in error. In this accelerating flow the viscous pressure distribution differs little from the inviscid ones, except on the leading half of the pressure surface where a cove separation bubble develops. McNally's Sasman-Cresci-type boundary layer code BLAYER[19] has been run for this blade using the panel pressure distribution. It does not predict the cove separation although the shape factors tend towards separation.

Inviscid and viscous Mach number contours in Figs. 15 and 16 show that the separation and wake have very little effect on the overall flow. Total pressure contours in Fig. 17 show that losses are confined to a very narrow region of the flow.

The cove separation bubble is clearly shown by the velocity vectors in Fig. 18. Although this separation has little apparent effect on the computed flow, it would cause a hot spot with possible thermal fatigue on the real blade. Furthermore, on a rotating turbine wheel the low-momentum fluid in the separation bubble would centrifuge to the tip where it would add to tip-clearance losses.

Figures 19 to 26 show results for a mid-span section of a core compressor rotor designated rotor 33. The actual compressor has a constant radius hub but the tip radius converges 3.5 percent. Here a mean mid-span radius of 215.5 mm (0.707 ft) has been used. At this radius the axial chord is 26 mm (.08532 ft), and the solidity is approximately one. At designed conditions the wheel speed is barely supersonic at mid-span.

The rotor has been tested experimentally by Strazisar et al.[20] using laser anemometry and conventional probe measurements. Performance measurements indicate that at a pressure ratio of 0.564 (exit static/inlet relative total) the flow is choked with an inlet relative Mach number of 1.271 at 60.8°. This is the case presented here. This case has also been computed with Thompkins' 3-D Euler code[21] by Chima et al.[22], where it was noted that the Euler results required a larger exit pressure than that measured.

The computations presented here were made on a 161 x 41 point grid using three levels of multiple-grid. Inviscid results converged in 2000 cycles taking 148 sec. Viscous results converged in 3500 cycles taking 475 sec.

The turbulent viscous solution was run at a Reynolds number of about 500 000 by specifing the measured y-velocity (wheel speed) upstream and measured pressure ratio of 0.564 downstream. The solution has an inlet Mach number of 1.295 (1.8 percent high) at 59.48° (1.32° low). Computed viscous Mach number contours shown in Fig. 19 may be compared with the experimental contours in Fig. 20. Both show a detached bow shock that intersects the suction surface near mid-chord. Both also show a diffuse compression to subsonic without a strong normal shock.

The Euler solution was computed with an increased pressure ratio of 0.656 (16.3 percent higher) such that the inviscid and viscous sonic lines (dashed contours) were coincident. The inviscid choked mass flow was 1.8 percent higher than the viscous mass flow. Computed inviscid Mach number contours shown in Fig. 21 may be compared to the 3-D Euler solution from[22] in Fig. 22. Both show reasonably good resolution of the bow wave system, but also show a strong normal shock attached to the trailing edge.

Figure 23 compares surface pressures from the present Euler solution (dashed line) to the 3-D Euler solution (circles). The 3-D solution used a sheared H-type grid with 100 x 17 points on each blade-to-blade plane and does not begin to resolve the stagnation point. The two Euler solutions agree reasonably well as to location and strength of the normal shock. However, the present solution predicts that the bow shock intersects the suction surface further aft than the 3-D solution. The Navier-Stokes solution (squares and triangles) agrees with the present Euler solution back roughly to the inviscid shock, but then shows a diffuse compression to a lower exit pressure.

Rotor 33 has round leading-and trailing edges with a radius of about 0.75 percent chord. Details of the viscous solutions in these regions are shown in Figs. 24 to 26. Figure 24 shows velocity vectors near the trailing edge. The suction surface flow separates at the passage "shock" and a thin region of reverse flow persists to the trailing edge. An interesting base recirculation region is also seen at the lower trailing edge. The viscous grid around the leading edge is shown in Fig. 25. Twenty-seven points are wrapped around the leading edge with an initial transverse spacing of 0.04 percent chord. Mach number contours in Fig. 26 show the computed bow shock standing off from the leading edge, the stagnation point, the development of the boundary layer, and the reacceleration of the external flow to supersonic speeds.

Concluding Remarks

An Euler and Navier-Stokes analysis code has been developed for turbomachinery cascades. The solution technique is based on the original explicit MacCormack algorithm. Computational efficiency has been achieved through use of variable time-step, a multiple-grid scheme, and by vectorization. The two acceleration schemes can reduce the CPU time of the original algorithm by a factor of about seven. The multiple-grid scheme is independent of the details of the fine-grid algorithm and as such may be applied directly to other Lax-Wendroff type algorithms.

Results have shown the method to be viable for low-speed to supersonic flows in widelyvarying cascade geometries. It has been shown that the code can predict subtle viscous flow phenomena that are not accounted for in current inviscid cascade analyses. Finally, the code is fast enough to be a useful tool in a turbomachinery design environment.

Acknowledgement

The author wishes to acknowledge the Low Speed Aircraft Research Branch and The Low Speed Wind Tunnel Investigations Branch from NASA Ames Research Center who provided the experimental data for the two wind tunnel turning vane cascades.

References

1. Katsanis, T., "FORTRAN Program for Calcultaing Transonic Velocities on a Blade-to-Blade Stream Surface of a Turbomachine," NASA TN D-5427, 1969.

2. Farrell, C., and Adamczyk, J., "Full Potential Solution of Transonic Quasi-3-D Flow Through a Cascade Using Artificial Compressibility," ASME Paper 81-GT-70, Mar. 1981.

3. Steger, J. L., Pulliam T. H., and Chima, R. V., "An Implicit Finite-Difference Code for Inviscid and Viscous Cascade Flow," AIAA Paper 80-1427, July 1980.

4. Shamroth, J., McDonald, H., and Briley, W. R., "Application of a Navier-Stokes Analysis to Transonic Cascade Flow Fields," ASME Paper 82-GT-235, Apr. 1982.

5. MacCormack, R. W., "The Effect of Viscosity in Hypervelocity Impact Cratering," AIAA Paper 69-354, Apr. 1969.

6. Ni, R. H., "A Multiple Grid Scheme for Solving the Euler Equations," AIAA Paper 81-1025, June 1981.

7. Johnson, G. M., "Multiple-Grid Acceleration of Lax-Wendroff Algorithms," NASA TM-82843, 1982.

8. Baldwin, B. S., and Lomax, H., "Thin-Layer Approximation and Algebraic Model for Separated Turbulent Flows," AIAA Paper 78-257, Jan. 1978.

9. Sorenson, R. L., "A Computer Program to Generate Two-Dimensional Grids About Airfoils and Other Shapes by the Use of Poisson's Equation," NASA TM-81198, 1980.

10. Steger, J. L., and Sorenson, R. L., "Automatic Mesh-Point Clustering Near a Boundary in Grid Generation with Elliptic Partial Differential Equations," Journal of Computational Physics, Vol. 33, No. 3, Dec. 1979, pp. 405-410.

11. Jameson, A., and Baker, T. J., "Solution of the Euler Equations for Complex Configurations," AIAA Paper 83-1929, July 1983.

12. Barton, J. T., and Pulliam, T. H., "Airfoil Computation at High Angles of Attack, Inviscid and Viscous Phenomena," AIAA Paper 84-0524, Jan. 1984.

13. Shang, J. S., "Numerical Simulation of Wing-Fuselage Aerodynamic Interaction," AIAA Paper 83-0225, Jan. 1983.

14. Johnson, G. M., "Convergence Acceleration of Viscous Flow Computations," NASA TM-83039, 1982.

15. Shang, J. S., Buning, P. G., Hankey, W. L., and Wirth, W. C., "The Performance of a Vectorized 3-D Navier-Stokes Code on the Cray-1 Computer," AIAA Paper 79-1448, July, 1979.

16. Chima, R. V., and Johnson, G. M., "Efficient Solution of the Euler and Navier-Stokes Equations with a Vectorized Multiple-Grid Algorithm," AIAA Paper 83-1893, July, 1983.

17. McFarland, E. R., "A Rapid Blade-to-Blade Solution for Use in Turbomachinery Design," NASA TM-83010, 1982.

18. Sanz, J. M., McFarland, E. R., Sanger, N. L., Gelder, T. F., and Cavicchi, R. H., "Design and Performance of a Fixed, Nonaccelerating, Guide Vane Cascade That Operates Over an Inlet Flow Angle Range of 60°," NASA TM-83519, 1984.

19. McNally, W. D., "FORTRAN Program for Calculating Compressible Laminar and Turbulent Boundary Layers in Arbitrary Pressure Gradients," NASA TN D-5681, 1970.

20. Strazisar, A. J., and Powell, J. A., "Laser Anemometer Measurements in a Transonic Axial Flow Compressor Rotor," Journal of Engineering for Power, Vol. 103 No. 2, Apr. 1981, pp. 430-437.

21. Thompkins, W. T., Jr., "A FORTRAN Program for Calculating Three-Dimensional, Inviscid, and Rotational Flows With Shock Waves in Axial Compressor Blade Rows: User's Manual," NASA CR-3560, 1982.

22. Chima, R. V., and Strazisar, A. J., "Comparison of Two-and Three-Dimensional Flow Computations With Laser Anemometer Measurements in a Transonic Compressor Rotor," NASA TP-1931, 1982.

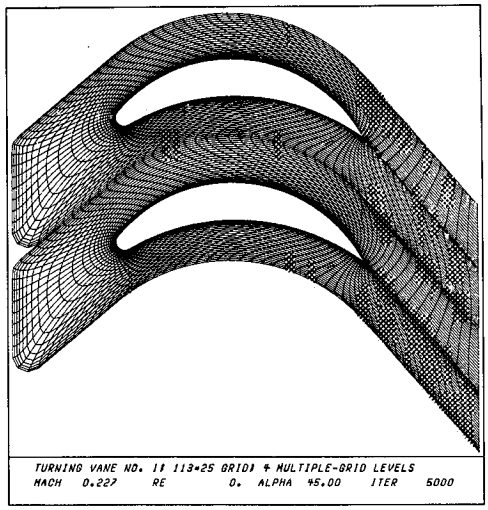

Figure 1. - Computational grid for 40' x 80' wind tunnel corner vane.

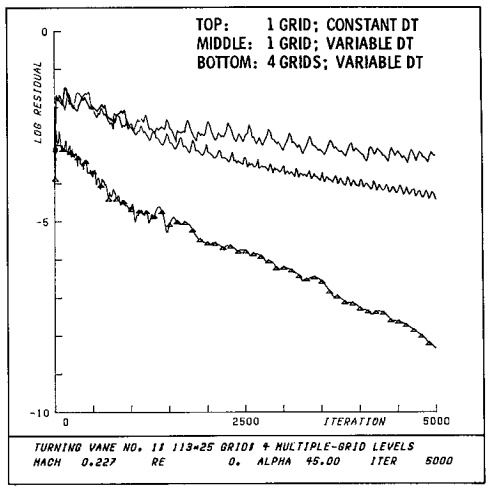

Figure 2. - Inviscid convergence histories for 40' x 80' wind tunnel corner vane.

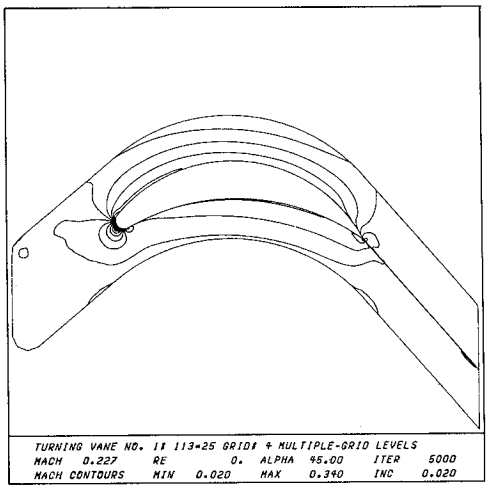

Figure 3. - Inviscid Mach number contours for 40' x 80' wind tunnel corner vane.

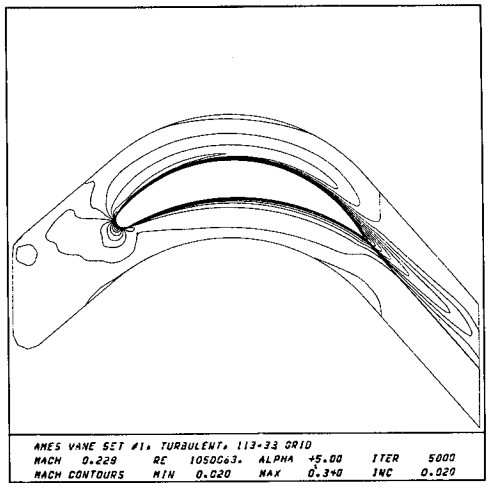

Figure 4. - Viscous Mach number contours for 40' x 80' wind tunnel corner vane.

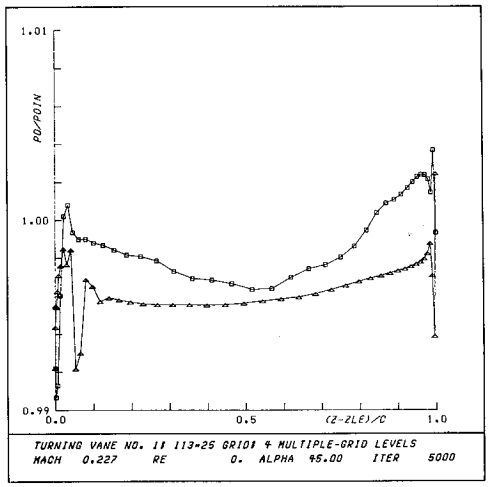

Figure 5. - Inviscid surface total pressures for 40' x 80' wind tunnel corner vane.

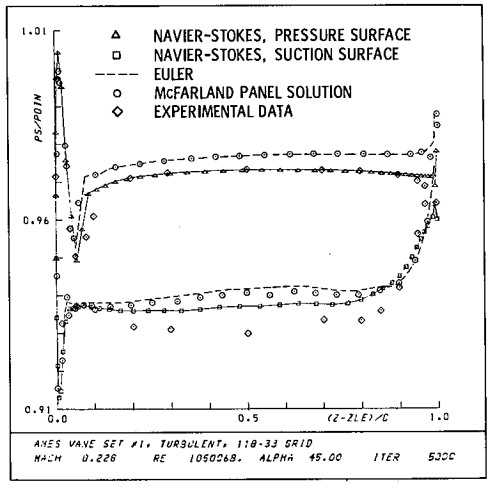

Figure 6. - Comparison of Euler, Navier-Stokes, and panel solutions with experimental data for 40' x 80' wind tunnel corner vane.

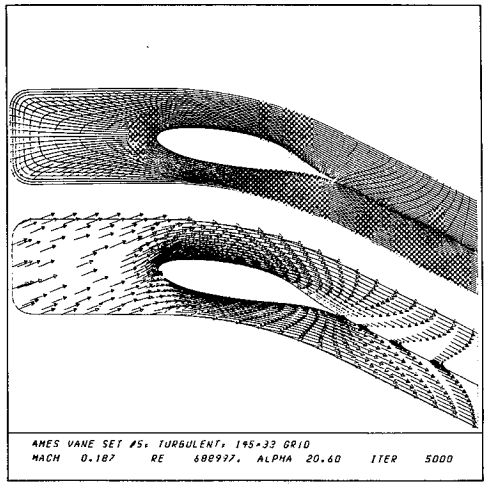

Figure 7. - Computational grid (top) and viscous velocity vectors (bottom) for wind tunnel turning vane, 80' x 120' mode.

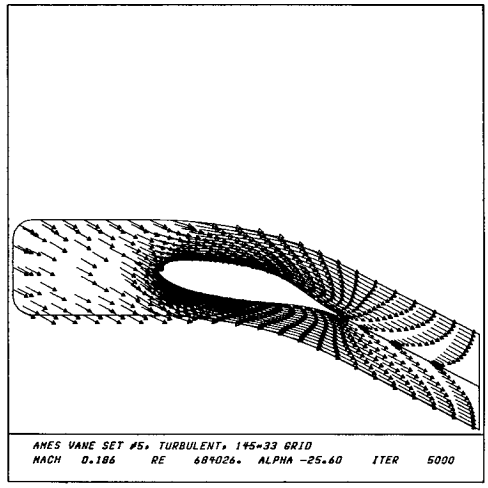

Figure 8. - Viscous velocity vectors for wind tunnel turning vane, 40' x 80' mode.

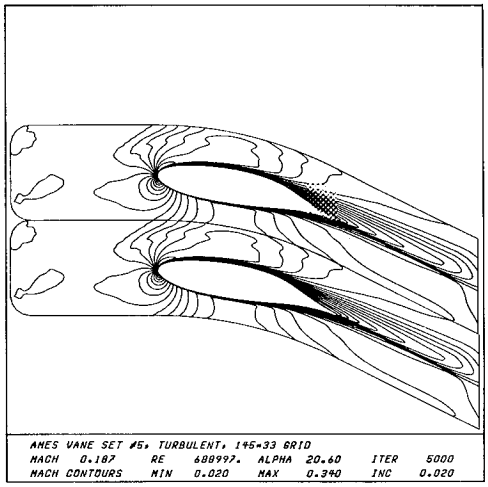

Figure 9. - Viscous Mach number contours for wind tunnel turning vane, 80' x 120' mode.

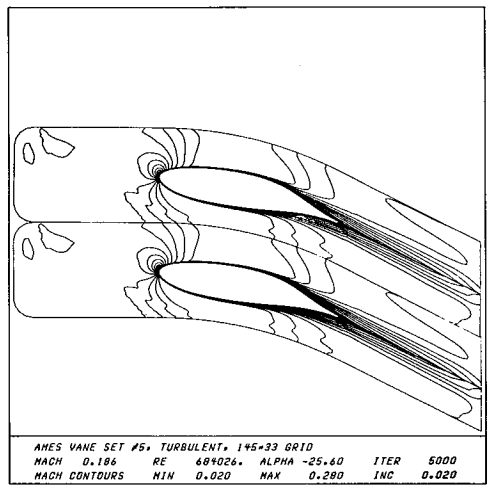

Figure 10. - Viscous Mach number contours for wind tunnel turning vane, 40' x 80' mode.

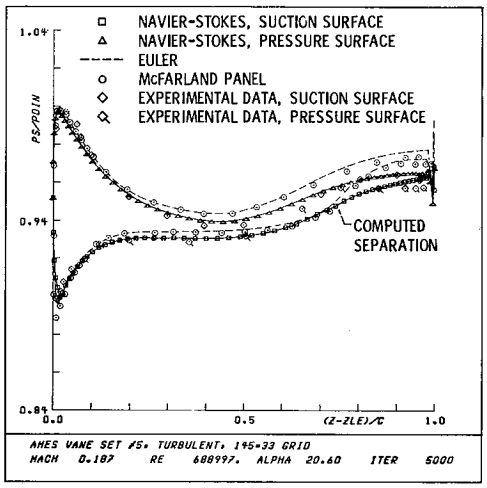

Figure 11. - Comparison of Euler, Navier-Stokes, and panel solutions with experimental data for wind tunnel turning vane, 80' x 120' mode.

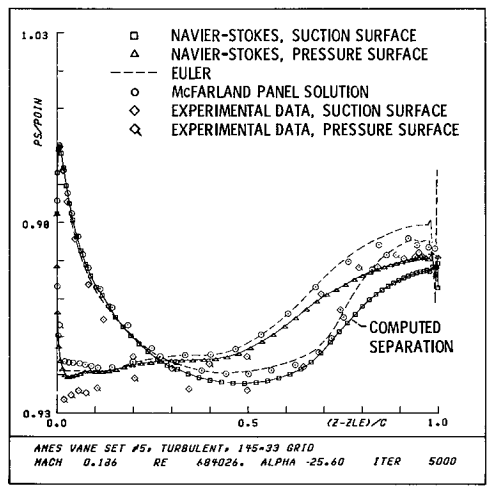

Figure 12. - Comparison of Euler, Navier-Stokes, and panel solutions with experimental data for wind tunnel turning vane, 40' x 80' mode.

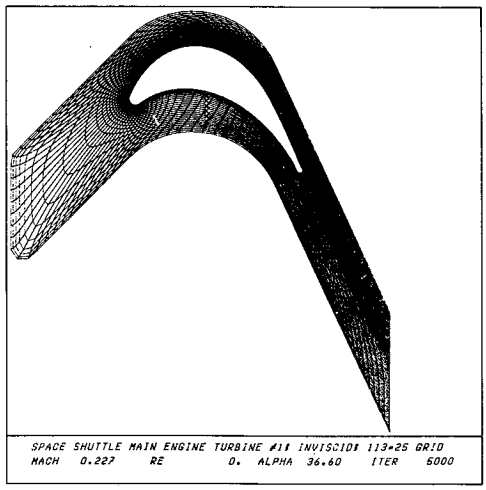

Figure 13. - Computational grid for space shuttle main engine fuel pump turbine rotor.

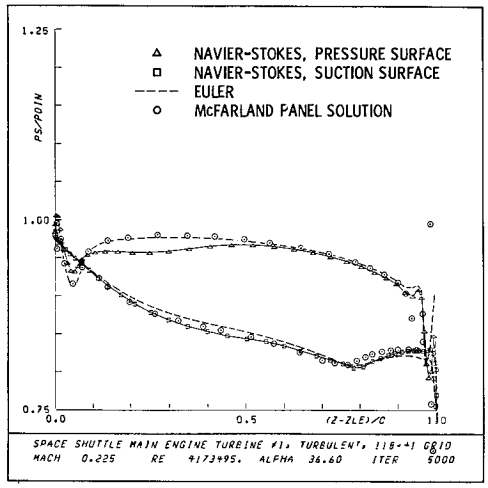

Figure 14. - Comparison of Euler, Navier-Stokes and panel solutions for space shuttle main engine fuel pump turbine rotor.

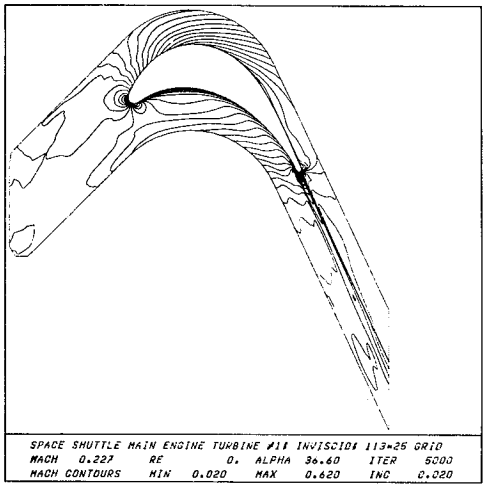

Figure 15. - Inviscid Mach number contours for space shuttle main engine fuel pump turbine rotor.

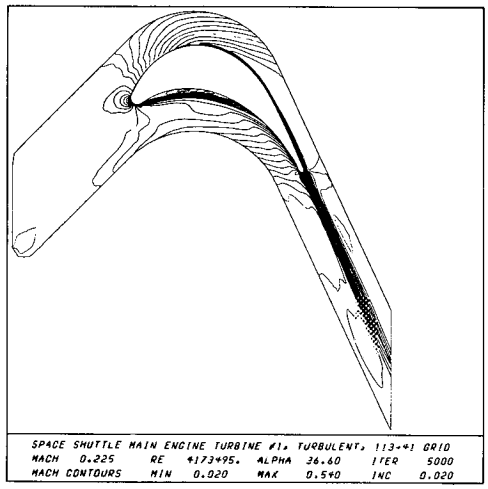

Figure 16. - Viscous Mach number contours for space shuttle main engine fuel pump turbine rotor.

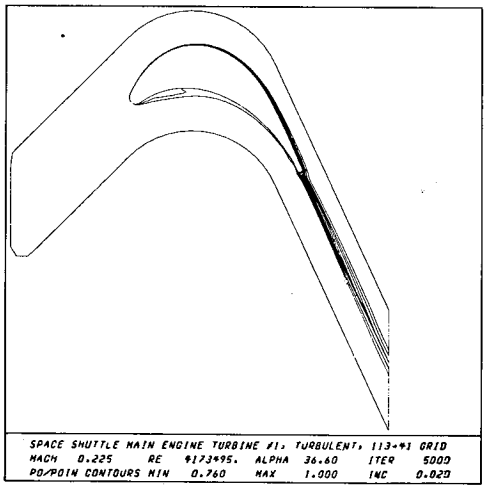

Figure 17. - Viscous total pressure contours for space shuttle main engine fuel pump turbine rotor.

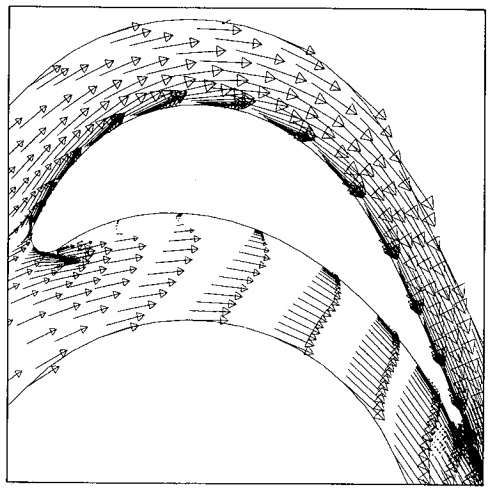

Figure 18. - Viscous velocity vectors for space shuttle main engine fuel pump turbine rotor.

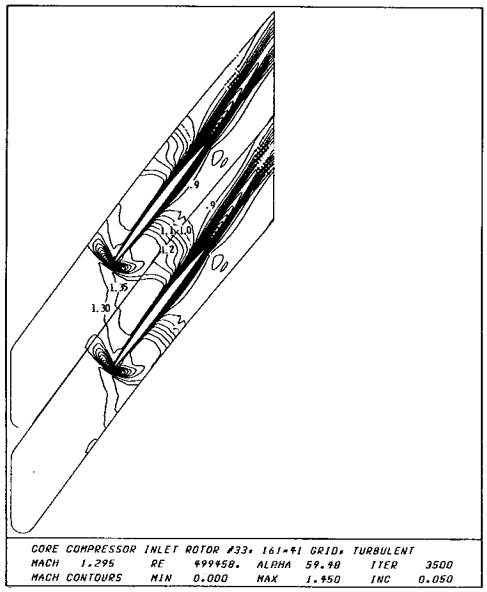

Figure 19. - Viscous Mach number contours for compressor rotor number 33, multiple-grid solution on mid-span section.

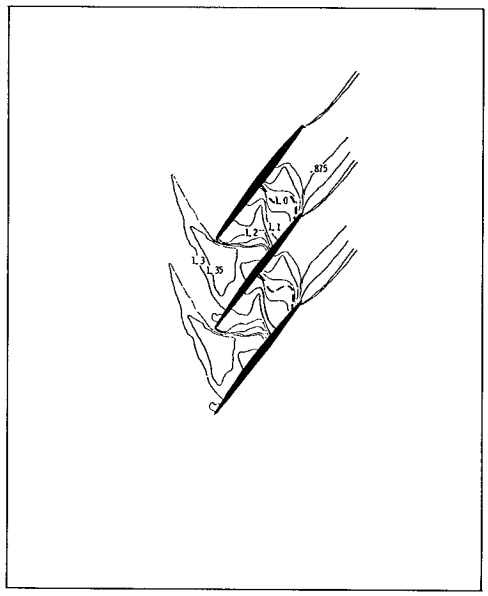

Figure 20. - Experimental Mach number contours for compressor rotor number 33, laser anemometry data on mid-span section.

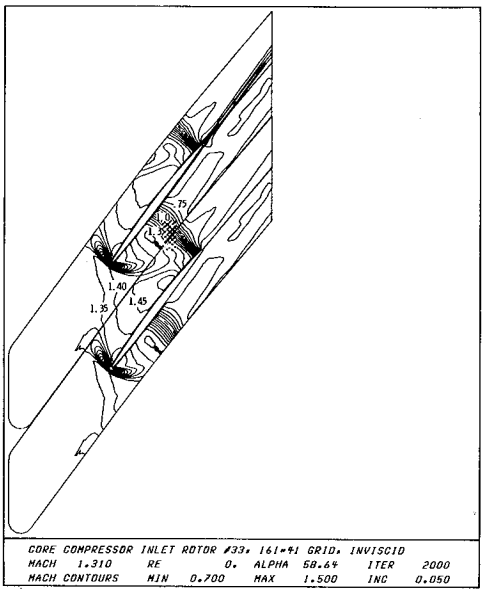

Figure 21. - Inviscid Mach number contours for compressor rotor number 33, multiple-grid solution on mid-span section.

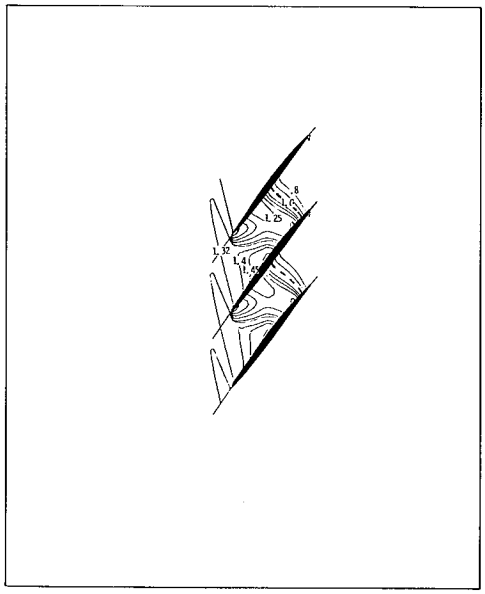

Figure 22. -Inviscid Mach number contours for compressor rotor number 33, 3-D Euler solution on mid-span section.

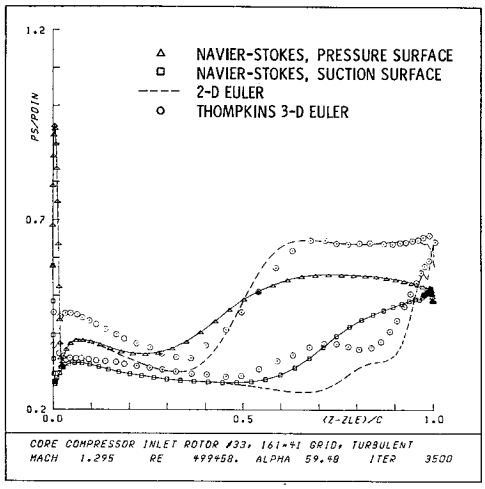

Figure 23. - Comparison of 2-D Euler and Navier-Stokes solution with 3-D Euler solution for compressor rotor number 33, mid-span section.

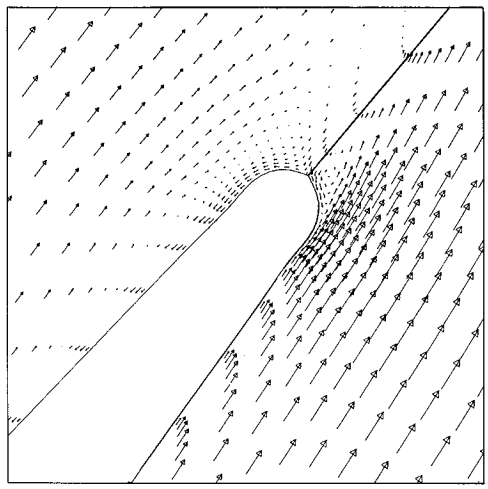

Figure 24. - Viscous velocity vectors about trailing edge of compressor rotor number 33, mid-span section.

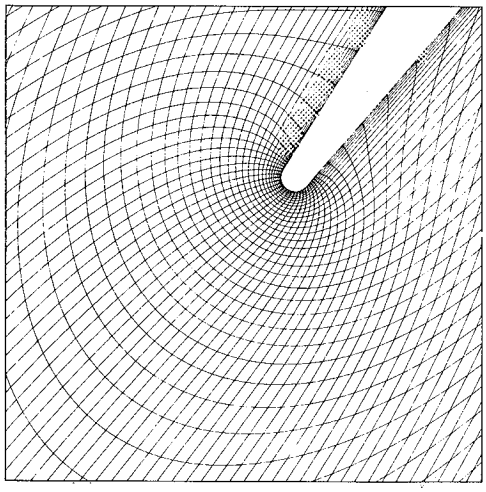

Figure 25. - Computational grid about leading edge of compressor rotor number 33, mid-span section.

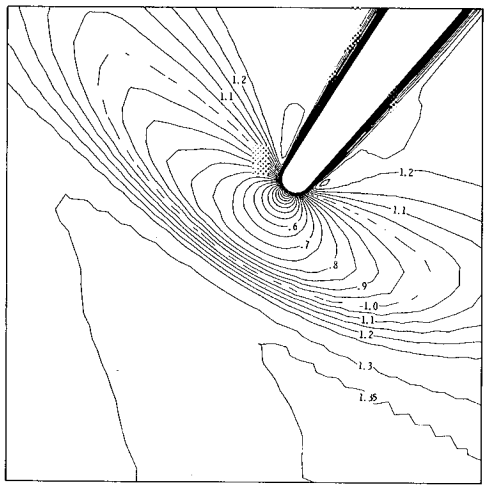

Figure 26. - Mach number contours about leading edge of compressor rotor number 33, mid-span section.

1. Report No.	2. Government Accession No.	3. Recipient's Catalog No.
NASA TM-83636		

4. Title and Subtitle	5. Report Date
Analysis of Inviscid and Viscous Flows in Cascades with an Explicit Multiple-Grid Algorithm	6. Performing Organization Code: 505-32-01

7. Author(s)	8. Performing Organization Report No.
Rodrick V. Chima	E-2078
	10. Work Unit No.

9. Performing Organization Name and Address	11. Contract or Grant No.
National Aeronautics and Space Administration Lewis Research Center Cleveland, Ohio 44135	13. Type of Report and Period Covered: Technical Memorandum

12. Sponsoring Agency Name and Address	14. Sponsoring Agency Code
National Aeronautics and Space Administration Washington, D.C. 20546	

15. Supplementary Notes

Prepared for the Seventeenth Fluid Dynamics, Plasma Dynamics, and Lasers Conference sponsored by the American Institute of Aeronautics and Astronautics, Snowmass, Colorado, June 25-27, 1984.

16. Abstract

A rapid technique has been developed for calculating inviscid and viscous flows in turbomachinery cascades. The Euler and thin-layer Navier-Stokes equations are solved using the original explicit MacCormack algorithm. The Baldwin-Lomax eddy viscosity model is used for turbulent flows. Convergence to a steady state is accelerated by use of a variable time-step and a multiple-grid scheme. Computer time is reduced through vectorization. Details of the numerical method are presented along with computed results for two low-speed wind tunnel turning vanes, a space shuttle fuel pump turbine rotor, and a supersonic inflow compressor rotor. Results show that the method can predict subtle viscous flow phenomena in cascades and is fast enough to be used as a design tool.

17. Key Words (Suggested by Author(s))		18. Distribution Statement
Euler equations Navier-Stokes equations Multiple-grid algorithm Inviscid flow Viscous flow	Turbomachinery Cascades	Unclassified - unlimited STAR Category 01

19. Security Classif. (of this report)	20. Security Classif. (of this page)	21. No. of pages	22. Price*
Unclassified	Unclassified		

*For sale by the National Technical Information Service, Springfield, Virginia 22161

National Aeronautics and
Space Administration

Washington, D.C.
20546

Official Business
Penalty for Private Use, $300

SPECIAL FOURTH CLASS MAIL
BOOK

Postage and Fees Paid
National Aeronautics and
Space Administration
NASA-451

NASA

POSTMASTER: If Undeliverable (Section 158
Postal Manual) Do Not Return